

Dual Modal Imaging-Guided Drug Delivery System for Combined Chemo-Photothermal Melanoma Therapy

Dong Zhang^{1-3,*}
Weifen Zhang^{1,2,*}
Xinghan Wu¹
Qian Li^{1,2}
Zhiyi Mu^{1,2}
Fengshuo Sun^{1,2}
Mogen Zhang¹
Guoyan Liu³
Linlin Hu^{1,2}

¹Shandong Engineering Research Center for Smart Materials and Regenerative Medicine, Weifang, 261053, People's Republic of China; ²College of Pharmacy, Weifang Medical University, Weifang, 261053, People's Republic of China; ³Department of Dermatology, Affiliated Hospital of Weifang Medical University, Weifang, 261031, People's Republic of China

*These authors contributed equally to this work

Purpose: Malignant melanoma is one of the most devastating types of cancer with rapid relapse and low survival rate. Novel strategies for melanoma treatment are currently needed to enhance therapeutic efficiency for this disease. In this study, we fabricated a multifunctional drug delivery system that incorporates dacarbazine (DTIC) and indocyanine green (ICG) into manganese-doped mesoporous silica nanoparticles (MSN(Mn)) coupled with magnetic resonance imaging (MRI) and photothermal imaging (PI), for achieving the superior antitumor effect of combined chemo-photothermal therapy.

Materials and Methods: MSN(Mn) were characterized in terms of size and structural properties, and drug loading and release efficiency MSN(Mn)-ICG/DTIC were analyzed by UV spectra. Photothermal imaging effect and MR imaging effect of MSN(Mn)-ICG/DTIC were detected by thermal imaging system and 3.0 T MRI scanner, respectively. Then, the combined chemo-phototherapy was verified in vitro and in vivo by morphological evaluation, ultrasonic and pathological evaluation.

Results: The as-synthesized MSN(Mn) were characterized as mesoporous spherical nanoparticles with 125.57 ± 5.96 nm. MSN(Mn)-ICG/DTIC have the function of drug loading-release which loading ratio of ICG and DTIC could reach to $34.25 \pm 2.20\%$ and $50.00 \pm 3.24\%$, and $32.68 \pm 2.10\%$ of DTIC was released, respectively. Manganese doping content could reach up to 65.09 ± 2.55 wt%, providing excellent imaging capability in vivo which the corresponding relaxation efficiency was $14.33 \text{ mM}^{-1} \text{ s}^{-1}$. And outstanding photothermal heating ability and stability highlighted the potential biomedical applicability of MSN(Mn)-ICG/DTIC to kill cancer cells. Experiments by A375 melanoma cells and tumor-bearing mice demonstrated that the compound MSN(Mn)-ICG/DTIC have excellent biocompatibility and our combined therapy platform delivered a superior antitumor effect compared to standalone treatment in vivo and in vitro.

Conclusion: Our findings demonstrate that composite MSN(Mn)-ICG/DTIC could serve as a multifunctional platform to achieve a highly effective chemo-photothermal combined therapy for melanoma treatment.

Keywords: Mn-doped mesoporous silica, drug delivery, magnetic resonance imaging, combination therapy

Introduction

Melanomas are among the most life-threatening skin malignancies. Concretely, although they account for only 4% of all types of skin cancers,¹ the odds of full recovery for melanoma patients is extremely low, and therefore melanoma accounts for 80% of all skin cancer mortalities. It is crucial to improve the success of patient

Correspondence: Guoyan Liu; Linlin Hu
Tel/Fax +86 15715369896
Email wliuguoyan@126.com; hull@wfm.c.edu.cn

treatment. Although numerous studies have explored alternative treatments for melanoma, few of them have achieved satisfactory effects to improve the overall survival of patients.² Therefore, novel and more effective therapeutic platforms are essential for melanoma treatment.

Chemotherapy is the earliest but still important treatment option. Dacarbazine (DTIC) is the only chemotherapeutic agent for melanomas that has been approved (in 1976) by the US Food and Drug Administration (FDA).³ However, its low water solubility results in a low and partial absorption rate, which limits its effectiveness in melanoma therapy.⁴ Moreover, DTIC is a non-specific drug and therefore also exhibits toxicity to healthy cells. The balance between efficiency and safety in chemotherapeutic agents is particularly challenging to achieve. Moreover, the lack of imaging guidance for therapeutic procedures can reduce efficiency. To address these drawbacks, a nanoparticle-based drug delivery system with multitherapeutic and imaging properties can be used as an effective approach.⁵

Various drug delivery nano-systems such as liposomes,⁶ copper particles,⁷ graphene oxide nanoparticles,⁸ and silica nanoparticles have been actively developed to improve the in vivo stability and pharmacokinetics of therapeutic compounds. Among these, mesoporous silica nanoparticles (MSNs) possess unique properties, such as controllable particle size and volume, outstanding loading capability, easy functionalization, and good biocompatibility, which makes them ideal nanocarriers for drug delivery and imaging.^{9,10}

Photothermal therapy (PTT) causes irreversible damage to cancer cells via the heat generated from the near-infrared (NIR) absorption of PTT materials, and therefore many studies have recently focused on this promising therapeutic strategy.^{11,12} Additionally, photothermal heating is also known to improve chemotherapy efficacy by enhancing the cellular uptake of chemotherapeutics and triggering intracellular drug release.^{13,14} Photodynamic therapy (PDT), employing a NIR laser to excite a photosensitizer to generate reactive oxygen species (ROS) and kill tumor cells. The co-delivery of chemotherapeutics and heat for synergistic melanoma treatment has great potential. Indocyanine green (ICG) is an ideal near-infrared light absorber for PTT and photosensitizer for PDT. Therefore, our study sought to load ICG and DTIC onto MSNs to assess the chemo-photothermal effects of this combined therapy. Moreover, the encapsulation of ICG in the MSNs could improve its stability and reduce its degradation rate. On the other hand, various imaging methods for physiological functions have attracted

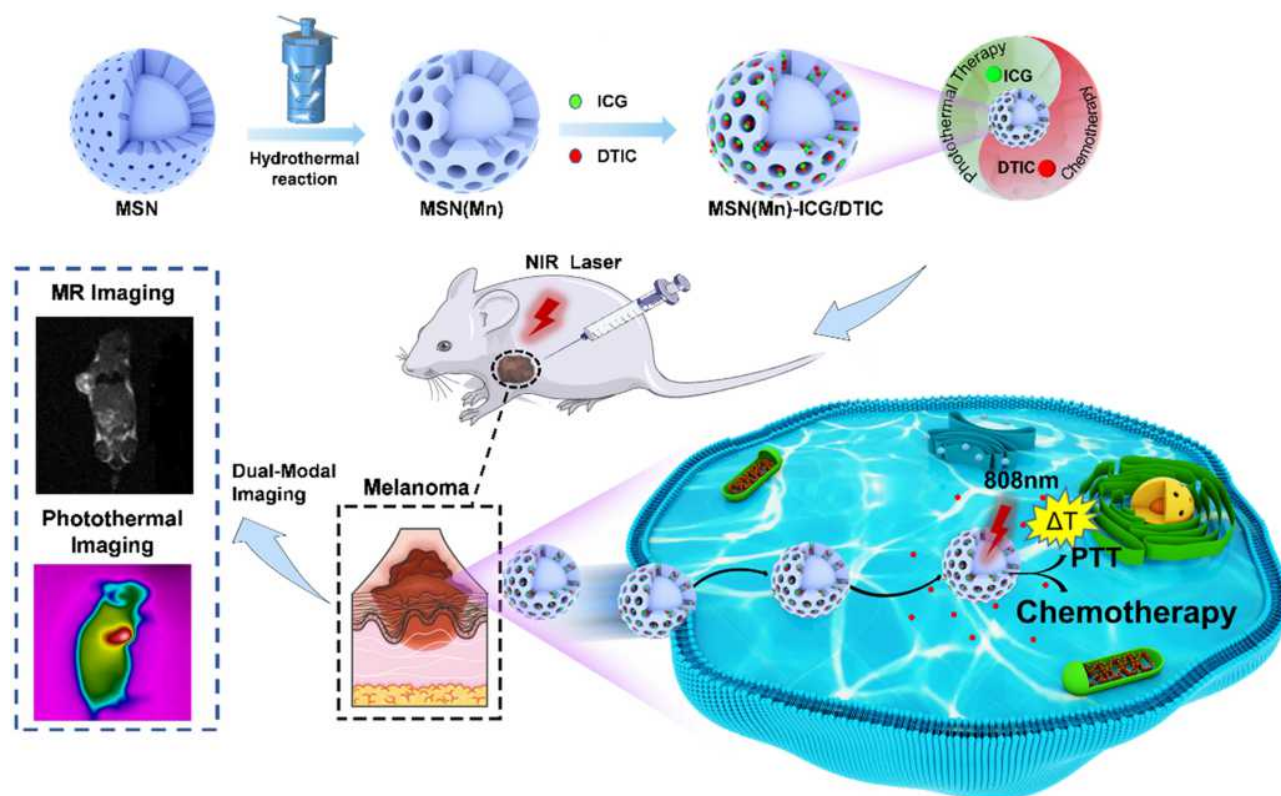
wide attention for guided therapy.^{15–18} Among these, magnetic resonance imaging (MRI) has several advantages, including its excellent temporal resolution, contrast, sensitivity, and safety. Most traditionally, gadolinium-based MRI contrast agents applied in clinics feature relatively low proton relaxation efficiency even at high concentrations (eg mM), thus resulting in toxicity risk.^{19,20} To address this problem, integration of metal ions, such as Mn, Zn, and Fe, in a nanoparticle system has recently been explored in vivo to enhance the quality of deep bioimaging.^{21–23} Manganese ion-doped mesoporous silica nanoparticles (MSN(Mn)) can either be applied for drug delivery or for imaging guidance.

Therefore, our study sought to develop an effective platform based on MSN(Mn), which provides excellent magnetic resonance and photothermal dual-mode imaging performance, thereby constituting a promising chemo-photothermal therapy for melanomas (Scheme 1). ICG (an NIR dye) and DTIC (a chemotherapeutic agent) were successfully loaded onto MSN(Mn), after which the photothermal effect and imaging capability of this combined system was tested, and the combination therapy was verified in vitro and in vivo. Importantly, our system features two unique characteristics compared to other previously reported nanocarriers for melanomas: (1) Mn-doped mesoporous silica exhibited a uniquely high r1 value which was beyond our expectations; (2) the MSN(Mn)-ICG/DTIC platform exhibited a remarkable synergistic therapeutic effect compared with ICG or DTIC treatment alone. Guided by MRI and PI, a combined chemo-photothermal melanoma therapy was successfully achieved. Thus, our findings demonstrate the potential applicability of multifunctional drug delivery systems as effective drug delivery and imaging agents for the combined treatment of melanoma.

Materials and Methods

Material

Cetyltrimethylammonium bromide (CTAB), tetraethyl orthosilicate (TEOS), triethanolamine (TEA), manganese sulfate monohydrate ($\text{MnSO}_4 \cdot \text{H}_2\text{O}$), disodium maleate, sodium hydroxide (NaOH), hydrochloric acid (HCl), ethanol, are purchased from Sinopharm Chemical Reagent Co., Ltd. (Shanghai, China), Indocyanine green (ICG), dacarbazine (DTIC) are obtained from Aladdin Reagents Co., Ltd. (Shanghai, China). Dulbecco's Modified Eagle Medium (DMEM), trypsin-EDTA, fetal bovine serum (FBS), 3-(4,5-dimethylthiazol-2-yl)-2, penicillin,



Scheme 1 Schematic diagram illustration about preparation of MSN(Mn)-ICG/DTIC and dual-mode imaging-guided combination chemotherapy and photothermal therapy.

streptomycin and 5-diphenyltetrazoliummerma bromide (MTT) assay kit are received from Nanjing KeyGEN Biotech Co., Ltd. (Nanjing, China). Annexin V-FITC and propidium iodide (PI) double staining cell apoptosis kit is received from BD Pharmingen (CA, USA). All reagents are of analytical reagent grade or the highest purity available and directly used without further purification. Deionized water of 18 MΩ cm is used throughout the experiments.

Animals

Female Balb/c nude mice with 5–6 weeks old were provided by the Beijing Vitong Lihua Laboratory Animal Technology Co., Ltd. (Beijing, China) and housed under specific pathogen-free conditions by the Experimental Animal Center, Weifang Medical University (Weifang, China). All of the animal experiments were conducted in strict accordance with the Guide for the Care and Use of Laboratory Animals published by the Weifang Medical University. The project was approved by the Animal Experimental Ethics Committee of Weifang Medical University. The treatment of experimental animals followed the 3Rs principle. All experiments follow the

ethical principles of experimental animal welfare and make every effort to minimize suffering.

Cells Line and Cells Culture

The A375 human melanoma cells line was obtained from Procell Life Science & Technology Co. Ltd. (Wuhan, China) and cultured in DMEM supplemented with 10% fetal bovine serum, 100 U/mL streptomycin and 100 U/mL penicillin. The cells were maintained at 37°C with 5% CO₂ in a humidified incubator. The medium was replaced every 2–3 days.

MSN(Mn) Synthesis and Doping

MSN(Mn) was synthesized in two steps: (1) synthesis of MSN via the sol-gel method and (2) doping of Mn into the MSNs framework via the hydrothermal process. The detailed procedures are shown in the [Supporting Information \(SI\)](#) (part 2).

Loading and Release

Photosensitizer ICG Loading

ICG, a NIR dye, is an FDA-approved photothermal agent. To achieve ICG loading, different volumes of ICG solution

(4.5 mg mL⁻¹ in DMSO) were mixed with 1.0 mg MSN(Mn) in 1.0 mL of phosphate buffer (PBS). At ICG concentrations of 100, 200, 300, 400, and 500 µg mL⁻¹, the corresponding mass ratios of ICG:MSN(Mn) were 0.2, 0.4, 0.6, 0.8, and 1.0. The mixture was then shaken for 24 h at room temperature and the obtained nanoparticles were collected by centrifugation. The ICG loading ratio (LR) was calculated by determining the absorbance at 780 nm of the supernatant filtrate. The product was then washed and re-suspended with PBS, then stored at 4 °C until required for downstream analyses. ICG LR is the mass ratio of ICG to MSN(Mn) adsorbed on MSN(Mn):

$$LR = (M_{ICG} - M_{UICG}) / M_{MSN(Mn)} \times 100\%$$

where M_{ICG} is the total mass of the added ICG; M_{UICG} is the mass of the ICG in the centrifugation supernatant; $M_{MSN(Mn)}$ is the mass of the added MSN(Mn).

Photosensitizer ICG Release

The release behavior of ICG was evaluated in 2.0 mL PBS (pH 7.4). The obtained MSN(Mn)-ICG was shaken at 37 °C in the dark, and 0.5 mL of the supernatant was recovered at different time points (3, 6, 12, 24, 48, and 72 h) after centrifuging. The release efficiency of ICG was calculated by determining the 780 nm absorbance of the supernatant filtrate. The MSN(Mn)-ICG was re-suspended with 0.5 mL of fresh PBS buffer for further releasing tests.

Drug DTIC Loading

DTIC (an effective chemotherapeutic agent for melanomas) was further loaded onto MSN(Mn)-ICG. To achieve this, 1.0 mg MSN(Mn)-ICG was mixed with different volumes of DTIC solution (2 mg mL⁻¹) to obtain different mass ratios (0.2, 0.4, 0.6, 0.8, and 1.0). The mixtures were diluted to 1.0 mL with pH 7.4 PBS buffer (pH 7.4) and shaken for 24 h at room temperature. MSN(Mn)-ICG/DTIC was obtained by centrifuging the mixtures and recovering the supernatant. The absorbance of the supernatant was measured at 323 nm and LF was calculated based on the Beer–Lambert law, in which LF is the mass ratio of DTIC to MSN(Mn)/DTIC. The calculation was conducted as follows:

$$LF (\%) = (W_{DTIC} - W_{TDTIC}) / W_{MSN(Mn)-ICG} \times 100\%$$

where W_{DTIC} is the total mass of DTIC added; W_{TDTIC} is the mass of DTIC in the centrifugation supernatant; $W_{MSN(Mn)-ICG}$ is the mass of the added MSN(Mn)-ICG.

DTIC Release

To study the DTIC release behavior, the MSN(Mn)-ICG/DTIC complexes were dispersed in 2.0 mL PBS at pH 7.4 and pH 5.5. The obtained complex was shaken at 37 °C in the dark, and 0.5 mL of the supernatant was moved out at different time points (3, 6, 12, 24, 48, and 72 h) after centrifuging. The absorbance of the supernatant was then detected at 323 nm with a spectrophotometer, after which the ICG release efficiency was calculated. The MSN(Mn)-ICG was then resuspended with 0.5 mL of fresh PBS buffer for further releasing tests.

Photothermal Properties, Photodynamic Effect and Photothermal Imaging

Photothermal agents can convert NIR light to heat energy, which is crucial to study the NIR absorption properties of ICG and evaluate its photothermal effects. Concretely, our study characterized the photothermal heating curves of ICG. Aqueous solutions of MSN, MSN(Mn), and MSN(Mn)-ICG/DTIC (1.0 mg mL⁻¹; pH 7.0) were placed in centrifuge tubes and analyzed with an infrared camera coupled with 808-nm laser at 0.8 W/cm². Equal volumes of PBS and ICG solution were used as controls. The temperature signals recorded at different time intervals (0, 1, 2, 3, 4, and 5 min) were analyzed with a photothermal imaging system. To verify the thermostability of ICG, MSN(Mn)-ICG/DTIC was irradiated for five cycles (15 min per cycle) with the aforementioned laser, after which the temperature was recorded.

NIR-laser with an 808 nm wavelength is used to perform the singlet oxygen generation (¹O₂) by the effect of photodynamic therapy (PDT). The generation of ¹O₂ is detected by using DPBF as a ¹O₂ sensor. Two millilitres of MSN(Mn), ICG and MSN(Mn)-ICG (60 µg mL⁻¹ for MSN(Mn) and 1 µg mL⁻¹ for ICG) in DMSO are mixed with 20 µL of DPBF (8 mM, DMSO), respectively. After stirring and irradiating using a NIR laser (808 nm; 0.8 W/cm²) for 10 min, the UV-vis absorption spectra of these mixtures are recorded.

To evaluate the photothermal effect of MSN(Mn)-ICG/DTIC, tumors were exposed to laser radiation, after which photothermal imaging was obtained by recording the temperature variation of the tumor. MSN(Mn)-ICG/DTIC (10 mg/kg for DTIC, 2.3 mg/kg for ICG) were injected into the tumor sites of mice, following irradiation with the 808-nm laser at 0.8 W/cm² for different time intervals (0, 1,

2, 3, 4, and 5 min). Thermal imaging was conducted with an IR thermal camera.

MR Imaging

Different amounts of MSN(Mn) nanoparticles were dispersed in DI water to obtain different Mn^{2+} concentrations (0.0225, 0.045, 0.09, 0.18, 0.36, and 0.72 mM). T1-weighted imaging of MSN(Mn)-ICG/DTIC suspensions was conducted under a 3.0 T MRI scanner (GE Signa, USA). Next, we explored the effect of MRI on the drug delivery system in mice. Nude BALB/C mice with subcutaneous A375 melanoma xenografts were used as models, and an MSN(Mn)-ICG/DTIC suspension ($2\text{ mg}\cdot\text{kg}^{-1}$) was intravenous injected into the mice ($n = 3$). T1-weighted animal MRIs were performed using an MRI scanner equipped with an animal coil. Images were collected before and after injection.

Cell Toxicity and in vitro Chemo-Phototherapy

The cell toxicity of MSN(Mn)-ICG was assessed by testing cell viability via the MTT assay. Various concentrations (0, 2.5, 5, 10, 20, 40, 80, and $160\ \mu\text{g mL}^{-1}$) of nanomaterials were incubated with A375 and HaCaT cells for 24 h. The untreated cells were selected as control groups. Afterward, $10\ \mu\text{L}$ of MTT solution was added to each well, followed by $100\ \mu\text{L}$ of dimethyl sulfite after 4 h. The absorbance at 490 nm was measured with a microplate reader after shaking for 10 min. The absorbance of the plate itself was recorded as a blank to assess the survival rate of cells in each experimental group [Cell survival rate = $(\text{OD experimental group} - \text{OD blank}) / (\text{OD control group} - \text{OD blank}) \times 100\%$].

Given the efficient phototherapy effects of MSN(Mn)-ICG/DTIC in vitro, the MTT assay was conducted to investigate its chemo-phototherapeutic effects in A375 cells. To achieve this, five groups were exposed to the following conditions: DTIC, DTIC + Laser, MSN(Mn)-ICG/DTIC, MSN(Mn)-ICG + Laser, MSN(Mn)-ICG/DTIC + Laser. The irradiation group was irradiated with NIR laser at different power levels (808 nm; 0.2, 0.4, 0.6, and $0.8\ \text{W}/\text{cm}^2$) for 20 min. Afterward, A375 cell viability was assessed via the above-described MTT method.

In addition, for cell apoptosis analysis, A375 cells, treated with DTIC, DTIC + Laser, MSN(Mn)-ICG/DTIC, MSN(Mn)-ICG + Laser, MSN(Mn)-ICG/DTIC + Laser,

were collected after trypsinization and washed in PBS. The irradiation group was irradiated with NIR laser (808 nm; $0.75\ \text{W}/\text{cm}^2$) for 10 min. Annexin V-FITC and propidium iodide (PI) double staining were used. Cell apoptosis was detected using the FACSuite on the BD FACSVerse system.

Combined Therapy for Cancer Treatment in vivo

To evaluate the efficacy of the combined therapy in vivo, male Balb/c nude mice with A375 melanoma tumors were bred. The tumor models in which the tumor volume reached approximately $50\ \text{mm}^3$ were divided into five groups (details provided below), and each group included five mice to assess the mean and standard deviation of the data.

Blank group (1): mice with injection of PBS and 808-nm laser exposure (laser only). Control group (2): mice with injection of MSN(Mn)-ICG/DTIC without 808-nm laser irradiation (MSN(Mn)-ICG/DTIC only); (3): mice with injection of MSN(Mn)-ICG with 808-nm laser irradiation (MSN(Mn)-ICG + Laser); (4): mice with injection of DTIC without laser exposure (DTIC only); treatment group (5): mice injected with the solution of MSN(Mn)-ICG/DTIC and exposed to 808-nm laser irradiation (MSN(Mn)-ICG/DTIC + Laser). All mice received drug solutions via intratumor injection every other day for 2 weeks (dose = 10 mg/kg for DTIC, 2.3 mg/kg for ICG). After injection for 4 hours, the animals of Group (1), (3), (4) and (5) were irradiated with 808-nm laser with a power density of $0.75\ \text{W}/\text{cm}^2$ for 10 minutes and then repeated irradiation once a day. After treatment, the sizes of the tumors were monitored every day for 14 days and determined by the following equation:

$$\text{Volume} = (\text{tumor length}) \times (\text{tumor width})^2/2.$$

Relative tumor volumes were calculated as V/V_0 (V_0 is the initial tumor volume). Additionally, the body weights and tumor weights of the mice were also evaluated for 14 days. The tumors were then stained with hematoxylin and eosin (H&E) to further evaluate toxicity. Finally, the therapeutic effect was further verified via ultrasound analysis by treating the tumor-bearing mice with MSN(Mn)-ICG/DTIC using the same amount of PBS injected in the control group.

Statistical Analysis

All data were statistically analyzed with SPSS 18.0 software. All values are presented as mean \pm SD. Parametric analyses performed by 2-tailed Student's *t*-test or one-way ANOVA and nonparametric analyses performed by Mann-Whitney *U*-test. *P*-value <0.05 was considered statistically significant in all cases (***p* < 0.01 ; ****p* < 0.001).

Results and Discussion

Characterizations

Our study developed an effective MRI- and PI-guided nanoplatform for melanoma treatment via chemical-photothermal combination therapy. Scheme 2 illustrates the fabrication procedure for the MSN(Mn)-ICG/DTIC nanocomplexes. First, MSN was synthesized via a typical sol-gel approach. Mn²⁺ was then doped onto the MSN framework under mild acidic and/or reducing conditions.¹⁹ The obtained MSN(Mn) has a unique morphologic structure and contrast-enhanced T1-weighted MIR capability for drug loading and imaging. ICG and DTIC were then loaded onto the MSN(Mn) to further assess their applicability in chemo-photothermal combination therapy.

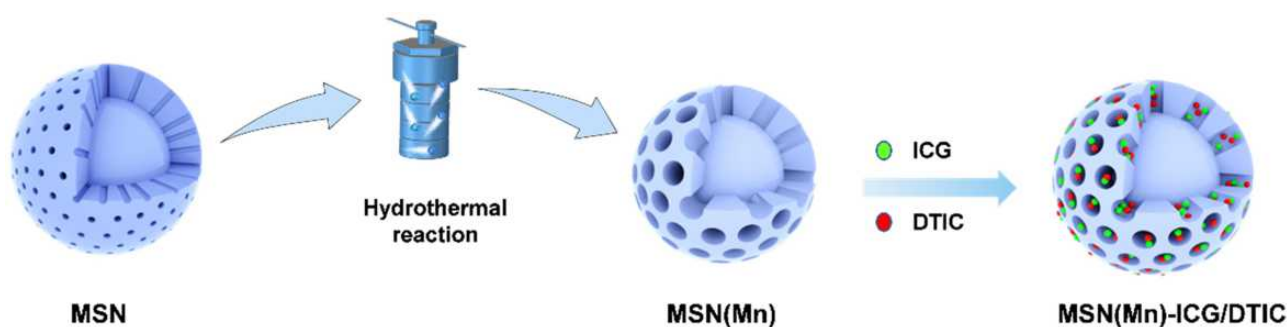
As-synthesized MSN was 154.33 \pm 5.06 nm with a polydispersity index (PDI) of 0.28, whereas that of the MSN(Mn) NPs was 125.57 \pm 5.96 nm with a PDI of 0.20. Zeta (ζ) potential was also used to monitor the preparation. After doping with Mn, the ζ potential of MSN(Mn) decreased from -9.36 ± 0.09 mV to -16.19 ± 0.20 mV (Figure S1). As shown in Figure 1A and B, the morphology of MSN and MSN(Mn) was analyzed via TEM. The as-synthesized MSN particles were characterized as mesoporous spherical nanoparticles with a well-defined mesoporous structure (Figure 1A). After hydrothermal treatment in an Mn precursor-containing solution, the MSN(Mn) surface became rough and exhibited large amounts of small nanobubbles on its surface,

which provides more space for drug loading (Figure 1B). The reason for the morphological changes of nanoparticles doped with manganese ions has been explored.^{24–27} Active sites were generated on the surface of MSNs because a small amount of silica hydrolyzed to H₄SiO₄ under hydrothermal condition, followed by adsorbing Mn²⁺ and carboxylate species via disodium maleate decomposition. The absorption of Mn²⁺ decreased the activation energy for the chemical decomposition of carboxylate, which decomposed into CO₂ and other gaseous species under hydrothermal treatment. In addition, the reaction between Mn²⁺ and H₄SiO₄ species resulted in Mn-doped silica deposition on the gas-liquid interface, forming solid nanospheres.

Then, the elemental distribution of MSN(Mn) was characterized via energy-dispersive spectrometer (EDS)-elemental mapping (Figure 1C and D). The desired elements [ie, Si (green), O (red), Mn (yellow)] were found to be spread homogeneously over the MSN, which further confirmed the homogenous distribution of Mn. The Mn content in MSN(Mn) was then further detected by inductively coupled plasma-mass spectrometry (ICP-MS), with values of up to 65.09 \pm 2.55 wt%.

As shown in the FTIR spectra in Figure 2A, the bands at around 1082cm⁻¹, 795 cm⁻¹ and 463 cm⁻¹ were attributed to the asymmetric stretching, symmetric stretching, and bending modes of Si-O-Si, respectively.²⁸ The peak at 960–970 cm⁻¹ is generally attributed to the stretching vibrations of a SiO₄ tetrahedron perturbed by the presence of a metallic group ensemble.²⁹ However, the MSN(Mn) band at 960 cm⁻¹ disappeared with the doping of Mn, which might suggest the incorporation of Mn into the silica framework (Mn-O-Si).³⁰

Moreover, XPS analysis of MSN(Mn) was also conducted to verify the valence state of Mn. As illustrated in Figure S2, our results validate the existence of the desired elements (ie, Si and O for MSN, and Si, O, and Mn for MSN(Mn)). Moreover, as shown in Figure 2B, the Mn 2p



Scheme 2 Construction of MSN(Mn)-ICG/DTIC.

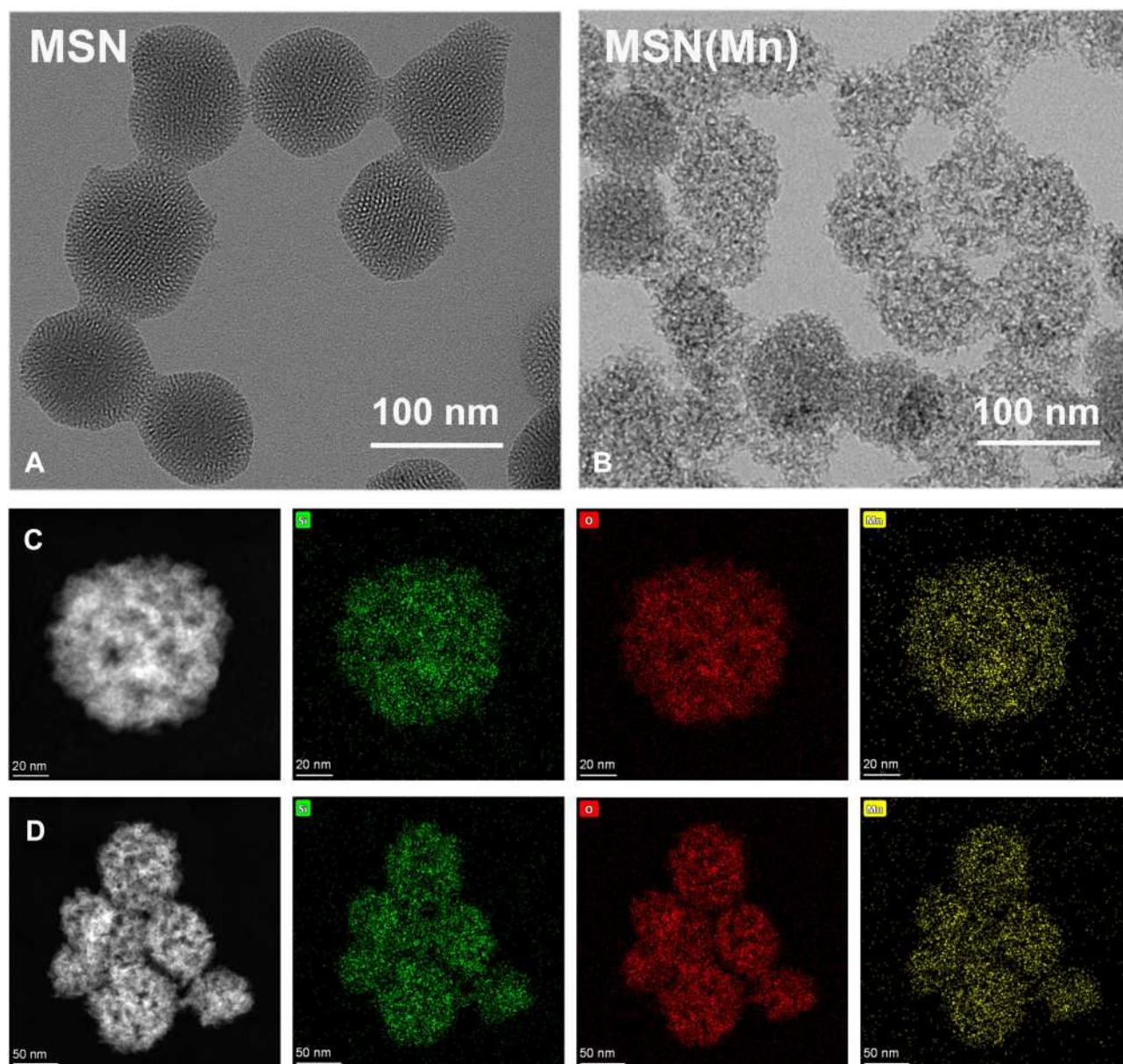


Figure 1 (A) TEM images of MSN (scale bar: 100 nm); (B) TEM images of MSN(Mn); (C) element mapping of a single MSN(Mn) sphere, (Si, O, and Mn are indicated in green, red, and yellow, respectively); (D) element mapping of multiple MSN(Mn) spheres.

orbital signal exhibited two peaks. The peak at 641.48 eV is attributed to the orbital of Mn 2p_{3/2},³¹ whereas the one at 658.08 eV represents the orbit of Mn 2p_{1/2}. The main peak of Mn 2p_{3/2} could be divided into three characteristic peaks at 641.2 eV, 642.3 eV, and 643.5 eV, corresponding to Mn²⁺, Mn³⁺, and Mn⁴⁺, respectively.³² Therefore, the XPS results confirmed that Mn was successfully doped into the MSN structure.

According to the N₂ absorption desorption isotherm and pore size distribution showed in Figure 2C and D, the as-

synthesized MSN exhibited a well-defined mesoporous structure with two distinct pore sizes of 2.1 and 3.2 nm. After doping with Mn, MSN(Mn) still exhibited a well-defined mesoporous structure. However, the 2.1 nm pores disappeared and the main pore size increased to 3.3 nm, which was consistent with the TEM images. Interestingly, the surface area, pore volume, and average pore size of MSN(Mn) increased, as summarized in Table S1. These results strongly suggest the occurrence of Mn components in the silica frame.

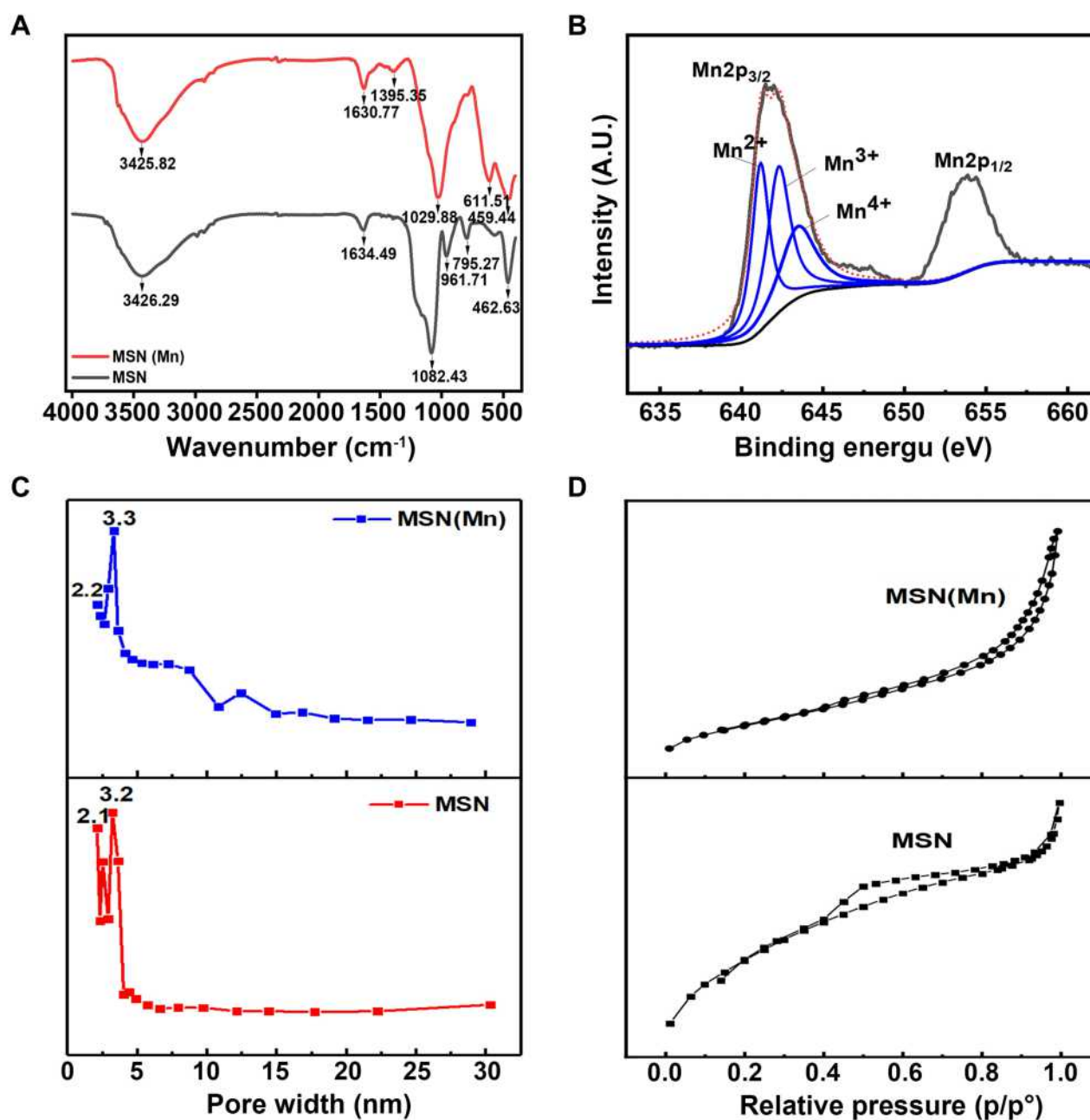


Figure 2 (A) FTIR spectrum of MSN and MSN(Mn); (B) XPS spectrum of MSN for Si 2p, O 1s, and Mn 2p; (C) BJH pore size distributions of MSN and MSN(Mn); (D) N₂ adsorption and desorption isotherms of MSN and MSN(Mn).

Loading and Release

Different drug ratios, ie, the mass ratio of the loaded ICG to MSN(Mn), can be easily obtained by mixing the components at different LRs and incubating the mixture in an aqueous solvent overnight. The loaded ICG is then steadily released from the complex. As shown in Figure 3A, the drug LR increases with the increase in the loaded amount of ICG. At an ICG

concentration above 400 mg mL⁻¹, the drug LR reaches a maximum value of 34.25±2.20%. The cumulative release profiles of ICG from MSN(Mn) in PBS at 37 °C are presented in Figure 3B, showing only a very small amount of loaded ICG (ie, 8.27±1.44%) released from MSN(Mn) after incubation with PBS buffer. However, this small loss would not affect the photo-thermal performance of ICG.

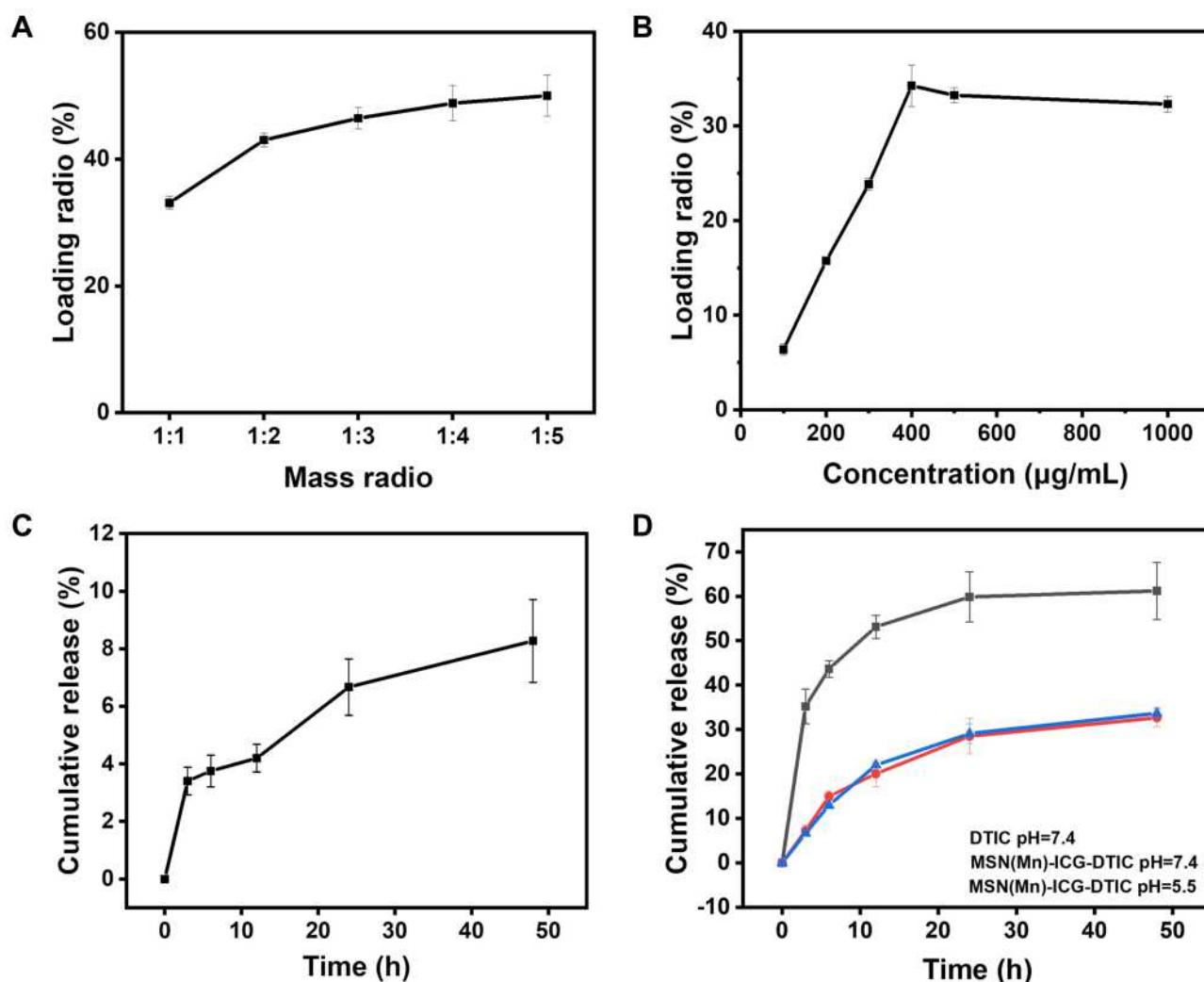


Figure 3 (A) Loading profile of ICG to MSN(Mn); (B) cumulative release profile of ICG to MSN(Mn); (C) loading profile of DTIC to MSN(Mn); (D) cumulative release profiles of DTIC to MSN(Mn) at different pH levels and pure DTIC.

Similarly, the loading efficiency of DTIC to MSN(Mn)-ICG was assessed by mixing the components at different mass ratios and allowing them to react overnight. As shown in Figure 3C, the loading of DTIC markedly increased with higher DTIC concentrations. By means of electrostatic interaction and hydrophobic interactions, DTIC can be loaded into nanoparticles with a high loading capacity of up to $50.00 \pm 3.24\%$ (DTIC/MSN(Mn)-ICG, w/w) at a mass ratio of 1:5. Loaded DTIC is then steadily released from the complex. Figure 3D illustrates the cumulative release profiles of DTIC from MSN(Mn) in PBS buffer with different pH values (7.4 and 5.5) at 37°C . A portion of the loaded DTIC ($32.68 \pm 2.10\%$) was released after incubation in PBS buffer for 48 h. However, the release behavior was barely affected by pH. As an insoluble drug, the

dissolution of pure DTIC was also examined. Here, we found that $61.23 \pm 6.42\%$ DTIC dissolved after 48 hours. These findings indicate that DTIC was released from the MSN(Mn), thus highlighting its effectiveness as a drug delivery system.

Photothermal Properties, Photodynamic Effect and Photothermal Imaging

The temperature increase generated by NIR laser irradiation is the most important parameter to evaluate the photothermal effect of the multifunctional drug delivery system developed herein. In our system, the temperature of MSN(Mn)-ICG/DTIC quickly increased by 25°C after laser irradiation for 5 min, whereas the temperature of nanoparticles without ICG could only increase by 8°C (Figure 4A). This result confirms that the photothermal conversion efficiency of this

drug delivery system was greatly enhanced by the inclusion of ICG. In contrast, the temperature of pure ICG began to decrease after 5 min, indicating an unstable photothermal effect. As shown in Figure 4C, after five 15-min cycles of irradiation, photothermal heating efficiency remained robust after five cycles of laser exposure. Therefore, our results demonstrated that ICG encapsulation in the drug delivery system could improve stability and reduce degradation rates.

Encouraged by the above-described photothermal effects, photothermal imaging was then conducted in vitro and in vivo. As shown in Figure 4B, the color of the photothermal images changed from black (corresponding to low temperature) to white (corresponding to high temperature), revealing a significant exposure time-dependent temperature rise. Under the same conditions, MSN(Mn)-ICG/DTIC also exhibited a brighter image, indicating a higher temperature compared with MSN and MSN(Mn). As shown in Figure 4D, after injecting MSN(Mn)-ICG/DTIC into the tumors,

the tumor temperature rapidly increased by 25 °C within 5 min, which was high enough to kill the melanoma cells but produced little damage to the surrounding normal tissues. Moreover, there was no significant difference between the mice injected with saline (control) after irradiation, thus demonstrating that the nanoparticles MSN(Mn)-ICG/DTIC played a crucial role in achieving photothermal heating and not the laser irradiation itself. This outstanding photothermal heating ability and stability highlighted the potential biomedical applicability of MSN(Mn)-ICG/DTIC as a PTT agent to kill cancer cells.

1,3-Diphenylisobenzofuran (DPBF) was selected as a probe to monitor the generated singlet oxygen to investigate the photodynamic effects of MSN(Mn)-ICG. As shown in Figure S3, after 10 min of irradiation, the UV absorption peak of NPs loading with ICG decreased obviously compared with blank nanoparticles. The absorption intensity of DPBF gradually decreased with

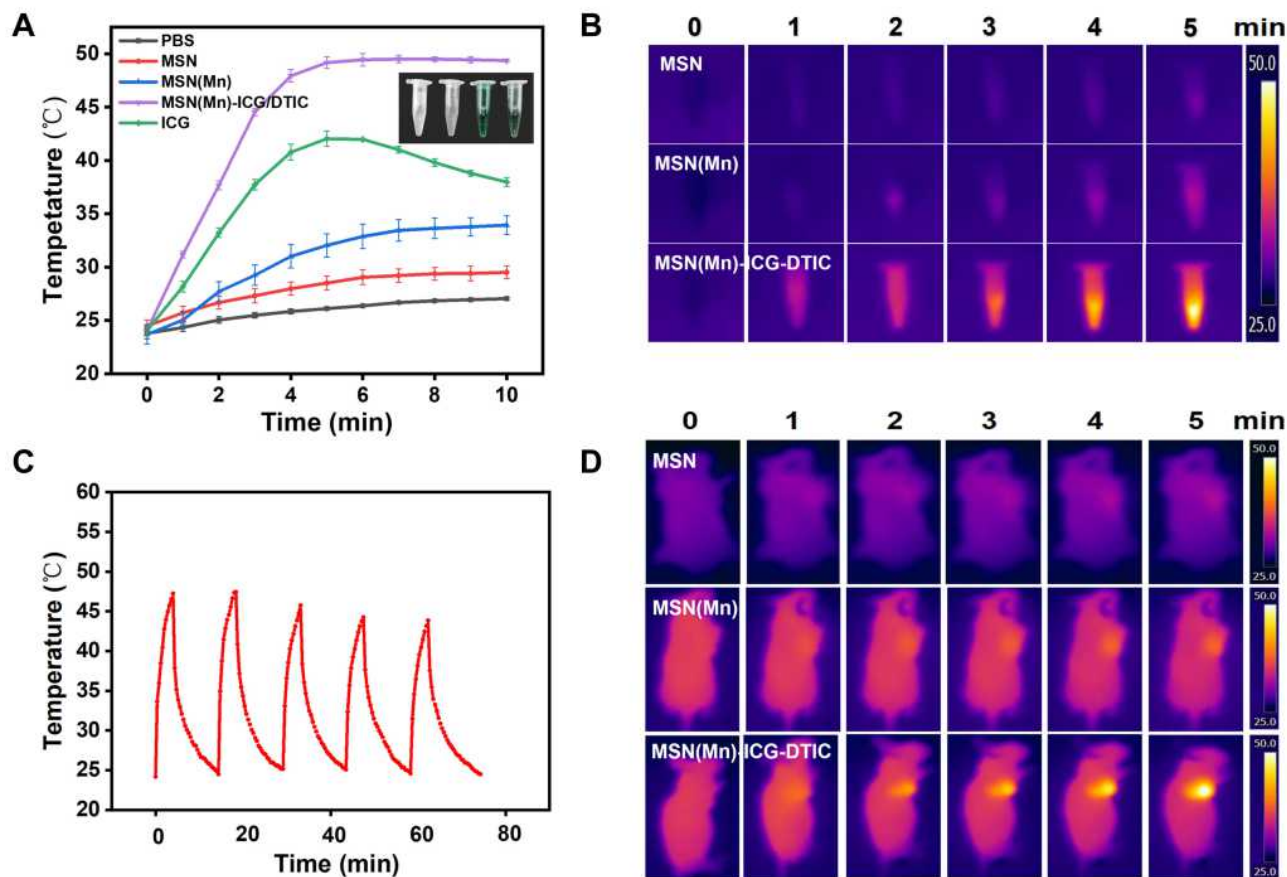


Figure 4 (A) PBS, MSN, MSN(Mn), MSN(Mn)-ICG/DTIC, and ICG time-dependent photothermal curves. (B) Photothermal images of MSN, MSN(Mn) and MSN(Mn)-ICG/DTIC after irradiation for different amounts of time. (C) Temperature changes of MSN(Mn)-ICG/DTIC under irradiation for five 15-min cycles. (D) Photothermal images of tumor-bearing mice injected with MSN, MSN(Mn) and MSN(Mn)-ICG/DTIC under irradiation for different amounts of time. Laser irradiation: 808 nm at 0.8 W/cm².

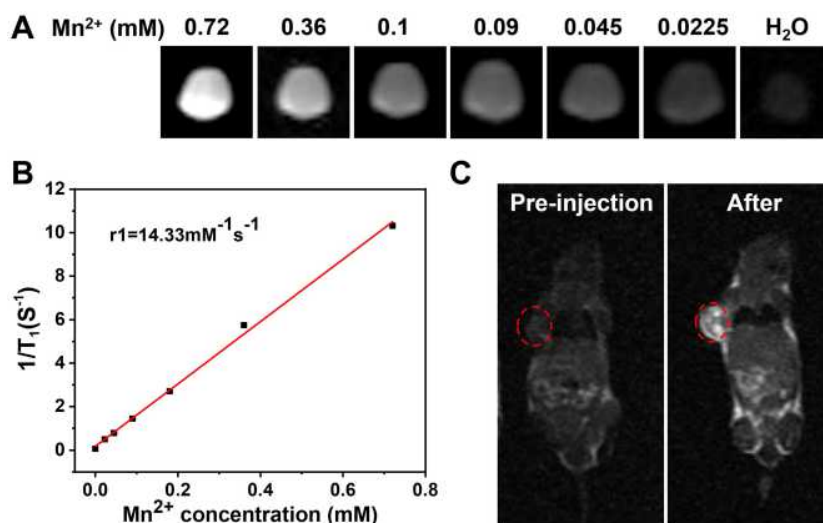


Figure 5 (A) T1-weighted MRI-signal intensity of solutions with different concentrations; (B) the T1 relaxation rates of MSN(Mn)-ICG/DTIC aqueous solutions with different Mn^{2+} concentrations; (C) In vivo T1-weighted MR images of mouse taken before injection and 4 h post i.v. injection with MSN(Mn)-ICG/DTIC. A brightening effect could be observed in the tumor region.

increasing irradiation time upon NIR laser irradiation, implying the continuous production of $^1\text{O}_2$ and excellent photodynamic effect of this nanoplatform.

MR Imaging

Mn^{2+} has been reportedly applied to MR imaging as a safe contrast agent. As shown in Figure 5A, MSN(Mn)-ICG/DTIC shows a significant concentration-dependent brightening effect under T1-weighted MRI. The linear relationship is shown in Figure 5B, and the longitudinal relaxivity coefficient (r_1) of MSN(Mn)-ICG/DTIC was calculated to be $14.33 \text{ mM}^{-1} \text{ s}^{-1}$, which is four times higher than that of

the commercially available agent Gd-DTPA ($4.40 \text{ mM}^{-1} \text{ s}^{-1}$).^{33,34} Therefore, our proposed system rendered superior MR contrast ability compared to other reported MRI agents, which are listed in Table 1. The excellent T1-weighted MRI effect observed herein may be due to the higher surface-to-volume ratio of MSN(Mn)-ICG/DTIC after doping due to an increase in water molecules coordinated with the metal ions (Mn^{2+}) in the doped material.³⁵

Encouraged by the excellent MRI properties of MSN(Mn)-ICG/DTIC in vitro, imaging capability was further evaluated in vivo. T1 images via intravenous injection of MSN(Mn)-ICG/DTIC in tumor-bearing mice are shown in Figure 5C. An obvious brightening effect was observed in the tumor site (marked by red circles) 4 h after injection compared with the pre-injected image. Our imaging results confirmed the specificity of the drug delivery system, as demonstrated by a localized accumulation in the tumor sites. Based on these positive results, we concluded that MSN(Mn)-ICG/DTIC was an effective nanoplatform for MRI and thermal imaging-guided tumor treatment.

Table 1 R_1 Relaxivity of MSN(Mn)-ICG/DTIC and Other Reported Regents

| Nanoparticles | Longitudinal Relaxivity r_1 ($\text{mM}^{-1} \text{ s}^{-1}$) | Reference |
|--|---|--------------|
| PEG/Mn-HMSNs | 2.46 | [24] |
| PDA-ICG-PEG/DOX(Mn) | 14.15 | [40] |
| $\text{Fe}_3\text{O}_4@ \text{Gd}_2\text{O}_3$ | 7.91 | [41] |
| CNMNs | 5.01 | [42] |
| $\text{Cu}_2\text{-xS@MnS}$ CSNPs | 1.243 | [43] |
| USMO@MSN | 5.61 | [44] |
| PMPDA NPs | 6.55 | [45] |
| HMONs-MnOx | 4.51 | [46] |
| $\text{Fe}_6\text{Gd}_6\text{P}_6$ | 2.7 | [47] |
| BPpb-HFI-Gd | 2.72 | [48] |
| Commercial Gd-DTPA | 4.40 | [33] |
| MSN(Mn)-ICG/DTIC | 14.33 | This article |

Cell Toxicity and in vitro Chemo-Photothermal Therapy

To investigate the intracellular therapeutic effect of the MSN(Mn)-ICG/DTIC drug delivery system, MTT assays were conducted to test the viability of A375 cells and HaCaT cells after incubation with various concentrations of MSN(Mn)-ICG/DTIC. No obvious cytotoxicity was observed after incubating the A375 cells and HaCaT

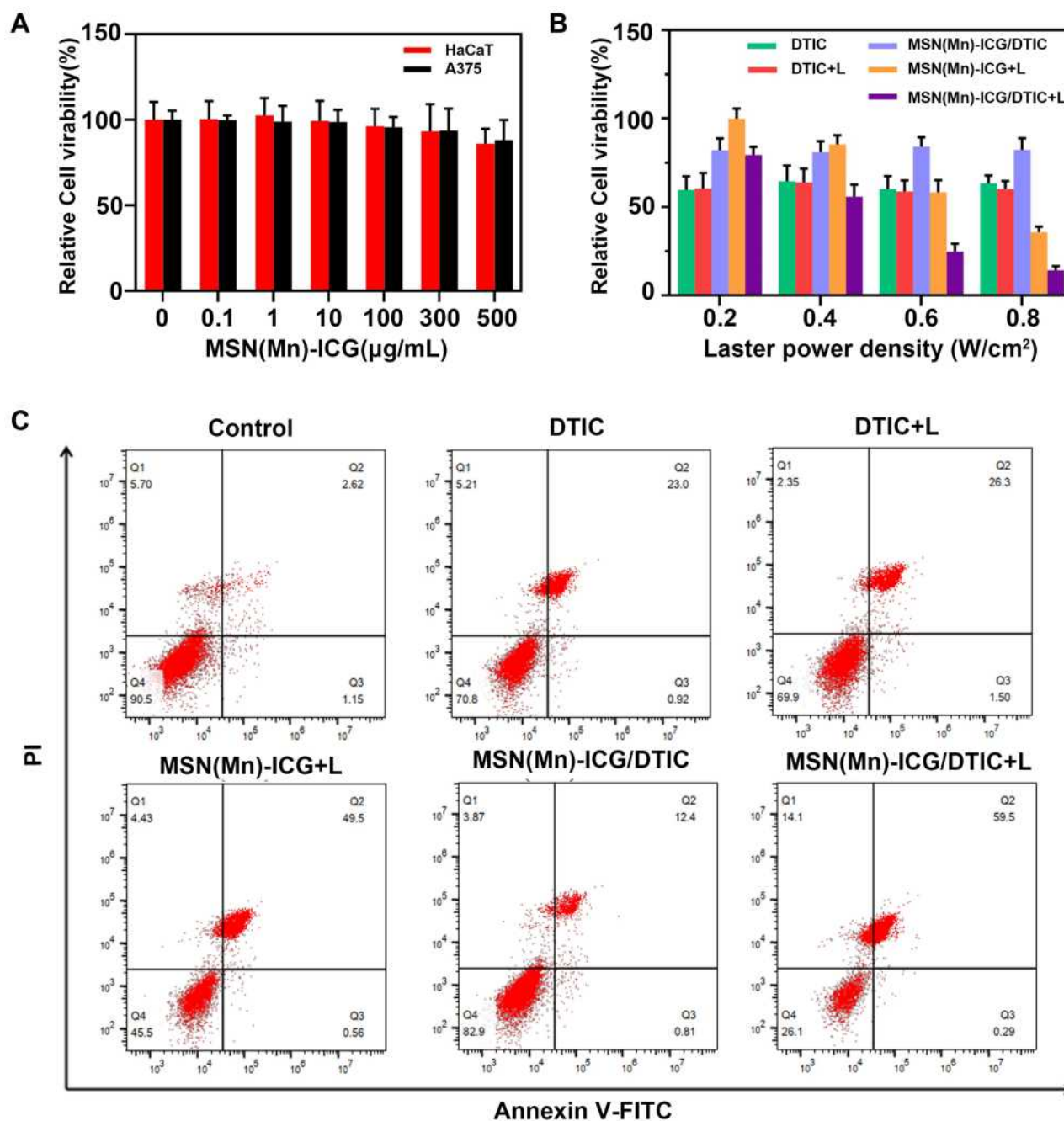


Figure 6 (A) Relative viabilities of HaCaT cells and A375 cells after being incubated with various concentrations of MSN(Mn)-ICG for 24 h; (B) relative viabilities of A375 cells after being incubated with DTIC, MSN(Mn)-ICG, and MSN(Mn)-ICG/DTIC with/without laser irradiation at different power densities (808 nm; 0.2, 0.4, 0.6, and 0.8 W/cm², 20min); (C) cell apoptosis and necrosis was analyzed via PI and annexin V-FITC staining when A375 cells were treated with DTIC, MSN(Mn)-ICG, and MSN(Mn)-ICG/DTIC with/without laser irradiation (808 nm, 0.75 W/cm², 10 min).

cells in up to 160 µg mL⁻¹ of MSN(Mn)-ICG for 24 h, which demonstrated the favorable biocompatibility of the nanocarriers (Figure 6A).

The MSN(Mn)-ICG/DTIC + Laser group (Figure 6B) exhibited remarkably lowest viabilities of A375 cells as the laser power densities increased from 0.2 to 0.8 W/cm², resulting in a synergistic effect between chemotherapy and

photothermal treatment. However, the chemotherapy-only group (treated with free DTIC at the same condition) exhibited low cytotoxicity, without any effect of laser exposure. Moreover, the photothermal effect from MSN(Mn)-ICG (ie, without chemotherapy) was also not as effective as the combined therapy. These results indicate that photothermal heating can not only kills cancer cells but also enhances

chemotherapy efficacy, which is consistent with previous studies.³⁶ Therefore, we conclude that combined therapy based on MSN(Mn)-ICG/DTIC exhibits excellent promising therapeutic effects for melanoma treatment in vivo.

To further confirm the effect of the synergistic group on the necrosis and apoptosis of A375 cells, the annexin V-FITC/PI apoptosis detection kit was used to assess the effects of different treated groups on the induction of apoptosis via FACSCalibur. The presence of necrosis (annexin V⁻, PI⁺) and apoptotic (annexin V⁺, PI[±]) cells was evaluated through flow cytometry and is shown in Figure 6C. MSN(Mn)-ICG/DTIC nanoparticles and Laser formulation caused a greater number of apoptosis than the control. A375 cells treated with nanoparticles and laser exhibited an apoptosis ratio higher than 59% after incubation for 24 h. Increased observed apoptosis may be attributed to intracellular ROS production. The ROS was

mainly generated by the ICG released from MSN(Mn)-ICG/DTIC within cells, ICG is a photosensitizer, used for photothermal therapy and photodynamic therapy of cancer. The apoptosis ratio was higher for the MSN(Mn)-ICG/DTIC + Laser group than the DTIC or the MSN(Mn)-ICG + Laser group, implying the co-delivery of nanoparticles produced a synergetic effect and promoted apoptosis in A375 cells, as reported previously.^{37,38} The result was consistent with the result of the MTT assay.

Combined Chemo-Photothermal Therapy in vivo

The in vivo antitumor efficacy of MSN(Mn)-ICG/DTIC was further investigated in melanoma tumor-bearing BALB/c mice. Mice with 50-mm³ tumor volumes were divided into five groups as shown in Figure 7A. After treatment, the tumors were collected for further analysis

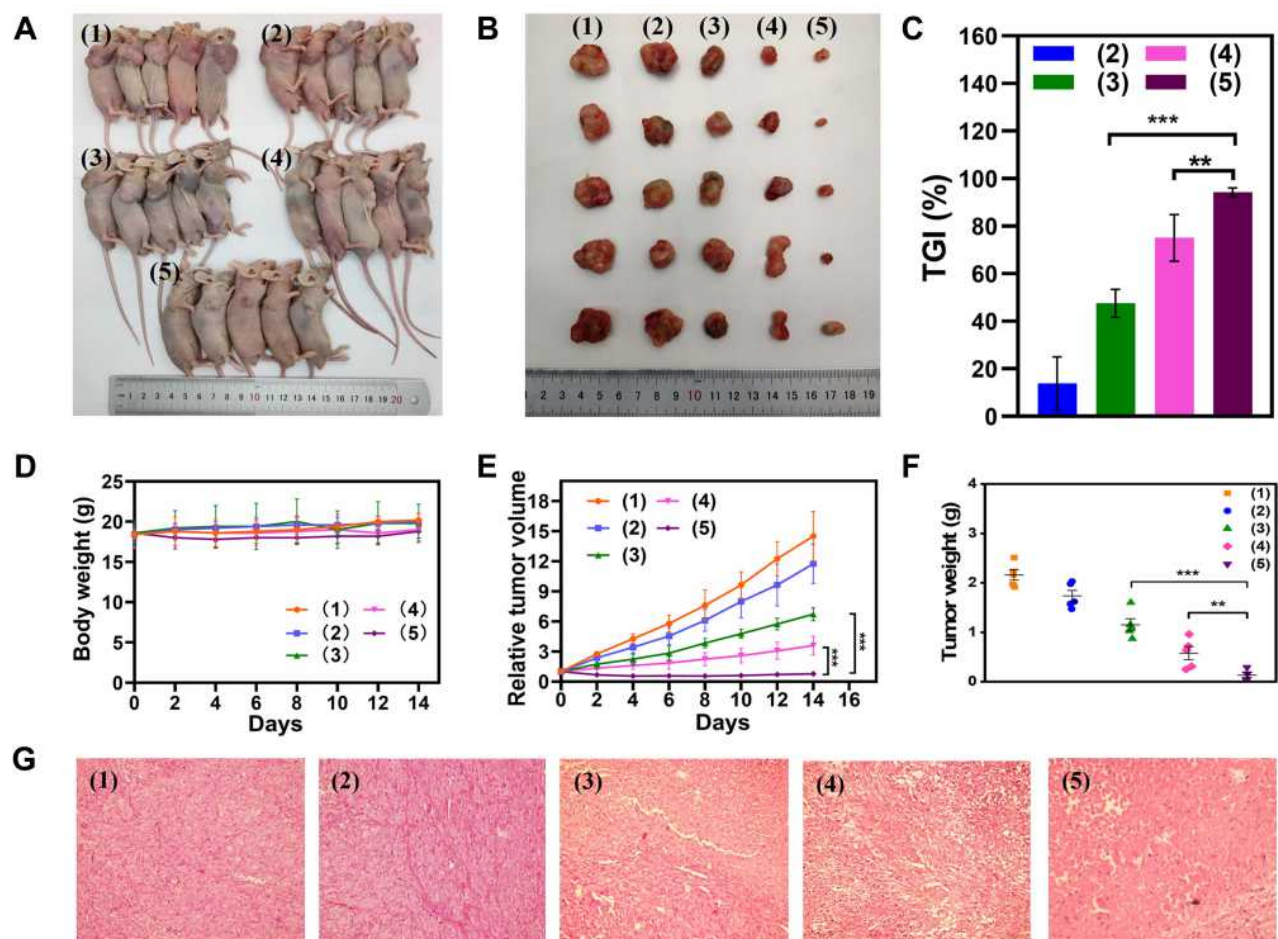


Figure 7 In vivo antitumor efficiency of A375 toward tumor-bearing BALB/c mice model. (A) The mice were intratumorally treated with (1) PBS + Laser; (2) MSN(Mn)-ICG/DTIC; (3) MSN(Mn)-ICG + Laser; (4) DTIC; or (5) MSN(Mn)-ICG/DTIC + Laser (808 nm, 0.75 W/cm², 10 min); (B) images of tumors stripped from mice after different treatments; (C) tumor volume growth curves with different treatments; (D) relative tumor volume; (E) TGI after treatment; (F) body weight changes of different groups; (G) H&E stain analysis of tumor sections after different treatments (***p* < 0.01; ****p* < 0.001).

on day 14, as shown in Figure 7B. The antitumor activity in mice was evident in terms of tumor size. The tumors in group 5 gradually shrank between days 2 and 14 at a faster rate than that of the other groups, demonstrating the outstanding antitumor activity of the proposed treatment. The tumor volumes in the blank group 1 increased throughout the entire experiment. The volume change curves of the tumors were measured once every 2 days during the 14-day period as shown in Figure 7C. On day 14, the relative tumor volume of group 5 was only approximately 5.81%, compared with 52.47% for group 3 and 24.89% for group 4. These findings highlight the superiority of the combined therapy. Moreover, the tumor weight of the treatment group was approximately 22.92% ($p < 0.01$) that of group 4 and 11.48% ($p < 0.001$) that of group 5 (Figure 7E), which also suggested that MSN(Mn)-ICG/DTIC had better therapeutic effects. At the same time, tumor growth inhibition (TGI) was calculated through tumor weight in Figure 7F, and the TGI of MSN(Mn)-ICG/DTIC reached values as high as 94.19%, representing the highest melanoma inhibition effects.

Systemic toxicity was evaluated based on body weight fluctuations. As shown in Figure 7D, small differences in body weight were observed between the treatment group and control groups, indicating that there was no significant systemic toxicity. The results of hematoxylin and eosin (H&E) staining also confirmed the therapeutic effect of the combined treatment (Figure 7G). The combination treatment group ((MSN(Mn)-ICG/DTIC with laser irradiation) exhibited much higher damage to tumor cells, whereas the other four groups showed little to no damage to tumor cells, which exhibited normal membrane morphology and nuclear structures. These observations are in close agreement with previous results,³⁹ thus confirming the excellent efficacy of the combined MSN(Mn)-ICG/DTIC treatment for melanoma inhibition.

Finally, the ultrasound results in Figure 8 show that the tumor treated with PBS + Laser was much larger than the tumor treated with (MSN(Mn)-ICG/DTIC + Laser, which was consistent with the above-described anticancer activities observed in vivo. These results further demonstrate that MSN(Mn)-ICG/DTIC exhibited a satisfactory therapeutic effect for melanoma treatment.

Conclusions

In summary, our study developed an innovative MSN(Mn)-ICG/DTIC-based strategy that combined MRI

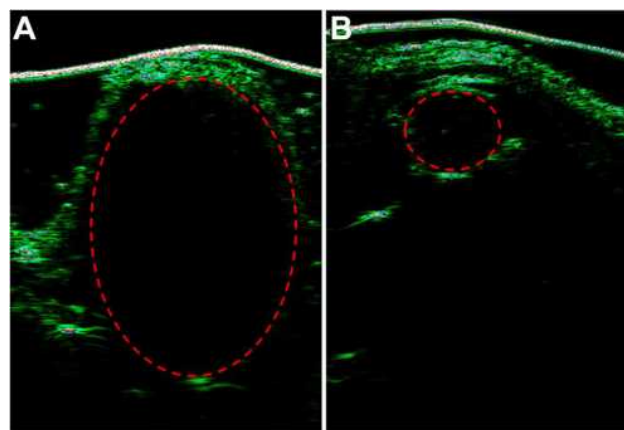


Figure 8 Ultrasounds of tumor-bearing mice treated with (A) PBS and (B) MSN(Mn)-ICG/DTIC.

and PI-guided (ie, chemo-photothermal) therapy to treat melanoma. In this work, MSN(Mn) exhibited great biocompatibility and multifunctional loading properties. ICG as a photothermal agent was absorbed by MSN(Mn) obtaining ICG- and DTIC-loaded MSN(Mn) which showed greatly enhanced photothermal conversion efficiency compared with free MSN(Mn) nanoparticles, as well as better photostability compared with free ICG. At the same time, DTIC can be adsorbed by MSN(Mn)-ICG nanoparticles for chemotherapy obtaining MSN(Mn)-ICG/DTIC which exhibits a superior antitumor effect compared with either chemotherapy or photothermal therapy, suggesting a synergistic effect in the combined treatment. In addition, chelation with Mn^{2+} ions further offered those nanoparticles great contrasts in MR imaging. Therefore, guided by precise dual-modal imaging, the proposed drug delivery system MSN(Mn)-ICG/DTIC offers a promising platform for the development of efficient drug delivery vehicles for melanoma therapy. The importance of studying the overall biological effects of nanomedicines has been widely recognized in this field. At present, the main focus of preclinical research is to evaluate the therapeutic efficacy of nanomedicines for proof-of-concept. However, in-depth in vivo analysis, including their long-term toxicity, cannot be overemphasized. Better in vitro settings to predict the biological activity of nanomedicines and the selection of the best drug candidates for further in vivo studies also seem to accelerate their clinical transformation.

Associated Content

*Supporting information

Supporting Information Available

Instrumentation; Synthetic procedures for MSN(Mn); Establishment of tumor xenograft on nude mice; Dynamic light scattering characterization of MSN and MSN(Mn); XPS spectra of MSN and MSN(Mn); UV-vis-NIR absorption spectra and the time-dependent variation of absorbance for free ICG, MSN(Mn), MSN(Mn)-ICG; Surface area, pore volume, and pore size of MSN and MSN(Mn).

Ethics Statement

The A375 cells were purchased from Procell Life Science & Technology Co., Ltd. The animal protocol was conducted according to the Guideline for the Care and Use of Laboratory Animals (NIH publication 85-23), and was approved by the Experimental Animal Ethics Committee of the Weifang Medical University.

Acknowledgments

The authors are indebted to the financial support from the National Natural Science Foundation of China (No. 81774125, 81973671), the major innovation and technology engineering project of Shandong Province (2019JZZY011106) and the international visiting project of Weifang Medical University.

Disclosure

The authors declare no competing financial interest in this work.

References

- Jemal A, Siegel R, Ward E, Murray T, Xu J, Thun MJ. Cancer statistics, 2007. *CA Cancer J Clin.* 2007;57:43–66. doi:10.3322/canjclin.57.1.43
- Ho H, Aruri J, Kapadia R, Mehr H, White MA, Ganesan AK. RhoJ regulates melanoma chemoresistance by suppressing pathways that sense DNA damage. *Cancer Res.* 2012;72:5516–5528. doi:10.1158/0008-5472.CAN-12-0775
- Kang M, Ren M, Li Y, Fu Y, Deng M, Li C. Exosome-mediated transfer of lncRNA PART1 induces gefitinib resistance in esophageal squamous cell carcinoma via functioning as a competing endogenous RNA. *J Exp Clin Cancer Res.* 2018;37:171. doi:10.1186/s13046-018-0845-9
- Tagne JB, Kakumanu S, Nicolosi RJ. Nanoemulsion preparations of the anticancer drug dacarbazine significantly increase its efficacy in a xenograft mouse melanoma model. *Mol Pharm.* 2008;5:1055–1063. doi:10.1021/mp8000556
- Mirsalari H, Maleki A, Raissi H, Soltanabadi A. Investigation of the pristine and functionalized carbon nanotubes as a delivery system for the anticancer drug dacarbazine: drug encapsulation. *J Pharm Sci.* 2021;110(5):2005–2016. doi:10.1016/j.xphs.2020.10.062
- Mishra H, Mishra PK, Iqbal Z, et al. Co-delivery of eugenol and dacarbazine by hyaluronic acid-coated liposomes for targeted inhibition of survivin in treatment of resistant metastatic melanoma. *Pharmaceutics.* 2019;11:163. doi:10.3390/pharmaceutics11040163
- Poudel K, Banstola A, Gautam M, et al. Macrophage-membrane-camouflaged disintegrable and excretable nanoconstruct for deep tumor penetration. *ACS Appl Mater Interfaces.* 2020;12:56767–56781. doi:10.1021/acsami.0c17235
- Poudel K, Banstola A, Tran TH, et al. Hyaluronic acid wreathed, trio-stimuli receptive and on-demand triggerable nanoconstruct for anchored combinatorial cancer therapy. *Carbohydr Polym.* 2020;249:116815. doi:10.1016/j.carbpol.2020.116815
- Iturrioz-Rodriguez N, Correa-Duarte MA, Fanarraga ML. Controlled drug delivery systems for cancer based on mesoporous silica nanoparticles. *Int J Nanomedicine.* 2019;14:3389–3401. doi:10.2147/IJN.S198848
- Tang F, Li L, Chen D. Mesoporous silica nanoparticles: synthesis, biocompatibility and drug delivery. *Adv Mater.* 2012;24:1504–1534. doi:10.1002/adma.201104763
- Xu J, Liu N, Wu D, Gao Z, Song YY, Schmuki P. Upconversion nanoparticle-assisted payload delivery from TiO₂ under near-infrared light irradiation for bacterial inactivation. *ACS Nano.* 2020;14:337–346. doi:10.1021/acsnano.9b05386
- Cheng L, Wang C, Feng L, Yang K, Liu Z. Functional nanomaterials for phototherapies of cancer. *Chem Rev.* 2014;114:10869–10939.
- Song G, Liang C, Gong H, et al. Core-shell MnSe@Bi₂Se₃ fabricated via a cation exchange method as novel nanotheranostics for multimodal imaging and synergistic thermoradiotherapy. *Adv Mater.* 2015;27:6110–6117. doi:10.1002/adma.201503006
- Zhang Z, Wang J, Chen C. Near-infrared light-mediated nanoplat-forms for cancer thermo-chemotherapy and optical imaging. *Adv Mater.* 2013;25:3869–3880. doi:10.1002/adma.201301890
- Chen B, Li C, Zhang J, et al. Sensing and imaging of mitochondrial viscosity in living cells using a red fluorescent probe with a long lifetime. *Chem Commun.* 2019;55:7410–7413. doi:10.1039/C9CC03977E
- Zhang C, Xie H, Zhan T, et al. A new mitochondrion targetable fluorescent probe for carbon monoxide-specific detection and live cell imaging. *Chem Commun.* 2019;55:9444–9447. doi:10.1039/C9CC03909K
- Szwargulski P, Wilmes M, Javidi E, et al. Monitoring intracranial cerebral hemorrhage using multicontrast real-time magnetic particle imaging. *ACS Nano.* 2020;14:13913–13923. doi:10.1021/acsnano.0c06326
- Wang J, Wang Z, Zhong Y, et al. Central metal-derived co-assembly of biomimetic GdTPP/ZnTPP porphyrin nanocomposites for enhanced dual-modal imaging-guided photodynamic therapy. *Biomaterials.* 2020;229:119576. doi:10.1016/j.biomaterials.2019.119576
- Wahsner J, Gale EM, Rodríguez-Rodríguez A, Caravan P. Chemistry of MRI contrast agents: current challenges and new frontiers. *Chem Rev.* 2019;119:957–1057. doi:10.1021/acs.chemrev.8b00363
- Layne KA, Wood DM, Dargan PI. Gadolinium-based contrast agents - what is the evidence for ‘gadolinium deposition disease’ and the use of chelation therapy? *Clin Toxicol.* 2020;58:151–160. doi:10.1080/15563650.2019.1681442
- Zhu W, Liu K, Sun X, et al. Mn²⁺-doped Prussian blue nanocubes for bimodal imaging and photothermal therapy with enhanced performance. *ACS Appl Mater Interfaces.* 2015;7:11575–11582. doi:10.1021/acsami.5b02510
- Fang W, Zhu W, Chen H, Zhang H, Zhao T. MRI enhancement and tumor targeted drug delivery using Zn²⁺-doped Fe₃O₄ core/mesoporous silica shell nanocomposites. *ACS Appl Bio Mater.* 2020;3(3):1690–1697. doi:10.1021/acsbam.9b01244
- Yang W, Xiang C, Xu Y, et al. Albumin-constrained large-scale synthesis of renal clearable ferrous sulfide quantum dots for T (1)-Weighted MR imaging and phototheranostics of tumors. *Biomaterials.* 2020;255:120186. doi:10.1016/j.biomaterials.2020.120186

24. Yu L, Chen Y, Wu M, et al. "Manganese extraction" strategy enables tumor-sensitive biodegradability and theranostics of nanoparticles. *J Am Chem Soc.* 2016;138:9881–9894. doi:10.1021/jacs.6b04299
25. Zhan G, Yec CC, Zeng HC. Mesoporous bubble-like manganese silicate as a versatile platform for design and synthesis of nanostructured catalysts. *Chemistry.* 2015;21:1882–1887. doi:10.1002/chem.201405697
26. Yec CC, Zeng HC. Nanobubbles within a microbubble: synthesis and self-assembly of hollow manganese silicate and its metal-doped derivatives. *ACS Nano.* 2014;8:6407–6416. doi:10.1021/nn501948h
27. Wang Y, Wang G, Wang H, Liang C, Cai W, Zhang L. Chemical-template synthesis of micro/nanoscale magnesium silicate hollow spheres for waste-water treatment. *Chemistry.* 2010;16:3497–3503. doi:10.1002/chem.200902799
28. Wang LZ, Shi JL, Yu J, Yan DS. Synthesis of nanostructured mesoporous silica materials containing manganese. *Nanostruct Mater.* 1998;10:1289–1299. doi:10.1016/S0965-9773(99)00009-4
29. Neau S, Prvulescu VI, Epure G, Preda E, Zecchina A. Photo-degradation of yperite over V, Fe and Mn-doped titania-silica photocatalysts. *Phys Chem Chem Phys.* 2008;10:6562–6570. doi:10.1039/b810200g
30. Tomer VK, Duhan S, Adhyapak PV, Mulla IS, Gouma P. Mn-loaded mesoporous silica nanocomposite: a highly efficient humidity sensor. *J Am Ceram Soc.* 2015;98:741–747. doi:10.1111/jace.13383
31. Dubal DP, Aradilla D, Bidan G, et al. 3D hierarchical assembly of ultrathin MnO₂ nanoflakes on silicon nanowires for high performance micro-supercapacitors in Li-doped ionic liquid. *Sci Rep.* 2015;5:9771. doi:10.1038/srep09771
32. Yang W, Su Z, Xu Z, Yang W, Li J. Comparative study of α -, β -, γ - and δ -MnO₂ on toluene oxidation: oxygen vacancies and reaction intermediates. *Appl Catal B.* 2019;260:118150. doi:10.1016/j.apcatb.2019.118150
33. Hu X, Tang Y, Hu Y, et al. Gadolinium-chelated conjugated polymer-based nanotheranostics for photoacoustic/magnetic resonance/NIR-II fluorescence imaging-guided cancer photothermal therapy. *Theranostics.* 2019;9:4168. doi:10.7150/thno.34390
34. Clough TJ, Jiang L, Wong KL, Long NJ. Ligand design strategies to increase stability of gadolinium-based magnetic resonance imaging contrast agents. *Nat Commun.* 2019;10. doi:10.1038/s41467-019-09342-3
35. Niu Y, Zhu J, Li Y, et al. Size shrinkable drug delivery nanosystems and priming the tumor microenvironment for deep intratumoral penetration of nanoparticles. *J Control Release.* 2018;35–47. doi:10.1016/j.jconrel.2018.03.012
36. Sherlock SP, Tabakman SM, Xie L, Dai H. Photothermally enhanced drug delivery by ultrasmall multifunctional FeCo/graphitic shell nanocrystals. *Acs Nano.* 2011;5:1505–1512. doi:10.1021/nn103415x
37. Poudel K, Banstola A, Gautam M, et al. Redox/photo dual-responsive, self-targeted, and photosensitizer-laden bismuth sulfide nanourchins for combination therapy in cancer. *Nanoscale.* 2021;13:1231–1247. doi:10.1039/D0NR07736D
38. Yu Y, Zhang Z, Wang Y, et al. A new NIR-triggered doxorubicin and photosensitizer indocyanine green co-delivery system for enhanced multidrug resistant cancer treatment through simultaneous chemo/photothermal/photodynamic therapy. *Acta Biomater.* 2017;59:170–180. doi:10.1016/j.actbio.2017.06.026
39. Jiang BP, Zhang L, Guo XL, Shen XC, Hong L. Poly (N-phenylglycine)-based nanoparticles as highly effective and targeted near-infrared photothermal therapy/photodynamic therapeutic agents for malignant melanoma. *Small.* 2016;13. doi:10.1002/smll.201602496
40. Dong Z, Gong H, Gao M, et al. Polydopamine nanoparticles as a versatile molecular loading platform to enable imaging-guided cancer combination therapy. *Theranostics.* 2016;6:1031–1042. doi:10.7150/thno.14431
41. Sun X, Du R, Zhang L, et al. A pH-responsive yolk-like nanoplat-form for tumor targeted dual-mode magnetic resonance imaging and chemotherapy. *ACS Nano.* 2017;11:7049–7059. doi:10.1021/acsnano.7b02675
42. Li J, Li X, Gong S, et al. Dual-mode avocado-like all-iron nanoplat-form for enhanced T(1)/T(2) MRI-guided cancer theranostic therapy. *Nano Lett.* 2020;20:4842–4849. doi:10.1021/acs.nanolett.0c00817
43. Huang X, Deng G, Han Y, et al. Right Cu(2-) (x) S@MnS core-shell nanoparticles as a photo/H(2)O(2)-responsive platform for effective cancer theranostics. *Adv Sci.* 2019;6:1901461. doi:10.1002/advs.201901461
44. Wang D, Lin H, Zhang G, et al. Effective pH-activated theranostic platform for synchronous magnetic resonance imaging diagnosis and chemotherapy. *ACS Appl Mater Interfaces.* 2018;10:31114–31123. doi:10.1021/acsami.8b11408
45. Miao ZH, Wang H, Yang H, Li ZL, Zhen L, Xu CY. Intrinsically Mn2 +-chelated polydopamine nanoparticles for simultaneous magnetic resonance imaging and photothermal ablation of cancer cells. *ACS Appl Mater Interfaces.* 2015;7:16946–16952. doi:10.1021/acscami.5b06265
46. Zhu P, Chen Y, Shi J. Nanoenzyme-augmented cancer sonodynamic therapy by catalytic tumor oxygenation. *ACS Nano.* 2018;12:3780–3795. doi:10.1021/acsnano.8b00999
47. Zhang Q, Wang P, Ling Y, et al. Single molecular Wells-Dawson-like heterometallic cluster for the in situ functionalization of ordered mesoporous carbon: AT1- and T2-weighted dual-mode magnetic resonance imaging agent and drug delivery system. *Adv Funct Mater.* 2017;27:1605313.
48. Ding Z, Cen J, Wu Y, et al. Self-Immolative nanoparticles for stimuli-triggered activation, covalent trapping and accumulation of in situ generated small molecule theranostic fragments. *Giant.* 2020;1:100012. doi:10.1016/j.giant.2020.100012

International Journal of Nanomedicine

Publish your work in this journal

The International Journal of Nanomedicine is an international, peer-reviewed journal focusing on the application of nanotechnology in diagnostics, therapeutics, and drug delivery systems throughout the biomedical field. This journal is indexed on PubMed Central, MedLine, CAS, SciSearch®, Current Contents®/Clinical Medicine,

Submit your manuscript here: <https://www.dovepress.com/international-journal-of-nanomedicine-journal>

Dovepress

Journal Citation Reports/Science Edition, EMBase, Scopus and the Elsevier Bibliographic databases. The manuscript management system is completely online and includes a very quick and fair peer-review system, which is all easy to use. Visit <http://www.dovepress.com/testimonials.php> to read real quotes from published authors.